

Multi-frame deconvolution with space-variant point spread functions by use of inverse filtering and Fast Fourier Transform

Mats G. Löfdahl*

*Institute for Solar Physics of the Royal Swedish Academy of Sciences
AlbaNova University Center, SE-106 91 Stockholm, Sweden*

A procedure for deconvolution of multiple images of the same object with space-variant point-spread functions (PSFs) is presented. It is based on expressing deconvolution with inverse filtering as convolution with kernels corresponding to inverse PSFs. Sets of basis functions are made from these inverse PSFs, given at discrete sample points, through Karhunen–Loève (K–L) decomposition. The entire field of view can then be convolved with the K–L kernels. Co-adding the results using continuous maps of expansion weights, interpolated for every pixel between the sample points, results in an image that is deconvolved with smoothly varying PSFs that match the discrete measurements. A demonstration data set is used to show how the transition between the grid points improves deconvolutions compared to piecewise deconvolution and mosaicking by avoiding the blending of discontinuities at the interfaces between adjacent subfields.

© 2008 Optical Society of America

OCIS codes: 100.0100, 100.1830, 100.2000, 100.3020.

1. Introduction

Deconvolution of images is much faster if the point-spread function (PSF) is invariant over the field of view (FOV) because the Fast Fourier Transform (FFT) can be used. However, in astronomical data from earth-bound telescopes, PSFs are frequently space-variant because of anisoplanatic seeing (field-dependent phase aberrations from atmospheric turbulence). Adaptive optics (AO) systems currently in use can correct optimally only in the isoplanatic patch close to the FOV of the wavefront sensor, so residual aberrations grow with distance from the sensor FOV.

Atmospheric wavefronts change significantly on time scales of 10^{-2} s, i.e., from one short-exposure to the next with current cameras. Anisoplanatism therefore has particular impact on multi-frame deconvolution. Even with perfect deblurring, geometrical distortions (from space-variant tilt components of the anisoplanatic seeing) that differ from frame to frame cause smearing from the co-adding of imperfectly registered structures. These effects have to be addressed for post-facto solar image restoration with Multi-Frame Blind Deconvolution (MFBD)¹, with or without Phase Diversity (PD)^{2,3} and Multiple Objects⁴. Space-variant PD image restoration has been demonstrated^{5,6} with algorithms that could probably be adapted for the other varieties of MFBD but is extremely time consuming. Compensating only partly for both the space-variant blurring and for the frame-to-frame variations in geometrical distortions, anisoplanatism is usu-

ally dealt with by processing subfields smaller than or on the order of the isoplanatic patch and mosaicking the results. This is also the usual procedure in solar speckle interferometry⁷. In effect, we are stitching together subfields restored by piecewise deconvolution in order to compensate for effects that are in reality changing continuously over the FOV. Overlapping subfields and tapered window functions are used to blur mismatches at the subfield borders but to our knowledge, there are no methods in practical use that address the problem of differential geometrical distortions *within* the subfields. The isoplanatic angle is on the order of $1''$ for a 1-meter telescope in very good seeing ($r_0 \approx 15$ cm), and is even smaller for worse seeing. One obvious remedy is to use smaller subfields but if the subfields are too small, there is not enough information to support estimation of the PSF.

In practice, for restoration of data from the Swedish 1-meter Solar Telescope (SST)⁸ with a FOV of $\sim 1'$, we have been using mosaicking of $5'' \times 5''$ subfields⁹. This means there are significant changes of the PSF shape within the subfields. In data collected in very good seeing conditions with the Swedish Vacuum Solar Telescope (SVST)¹⁰, the predecessor of the SST, we have observed effects of differential geometric effects within a subfield of similar size¹¹.

Deconvolution with space-variant PSFs has been addressed for night-time astronomy in several papers. Because night-time observations most often result in high-contrast images with intensity-dependent noise, deconvolution methods used tend to be of the conditional probability kind, such as Lucy–Richardson, where the deconvolution is never calculated explicitly. Using long exposures, the PSFs usually have a simple structure and often vary over the FOV mainly with the distance from the AO

*Electronic address: mats@astro.su.se

sensor FOV. The state of art in 1997 is summarized in Ref. 12.

Recently, a procedure for space-variant Lucy–Richardson was presented¹³, based on two ideas found in the literature. The first idea¹⁴ is the convolution of large FOVs with space-invariant kernels used as basis functions in expansions of sample space-variant PSFs. Combining the different convolved contributions using continuously varying weights, that are interpolated between the sample points, captures the spatial variations. The second idea, a Karhunen–Loève (K–L) decomposition of the space-variant PSFs, making optimal basis functions for each set of PSFs, is found in Ref. 15.

In this paper, we adapt the space-variant Lucy–Richardson procedure¹³ to deconvolution by inverse filtering of multi-frame data. Our own motivation for developing such an algorithm is the deconvolution of high-resolution solar images, and such a data set is used for demonstrating the use of the algorithm. However, the algorithm is quite general and should be useful in other situations, where one needs to improve resolution and signal to noise ratio (SNR) by combining multiple, short-exposure, Gaussian noise data frames with distinct and space-variant PSFs, including differential distortion effects.

2. Theory

A. Deconvolution as decomposed convolution

In an isoplanatic image formation model, valid for a subfield smaller than the isoplanatic patch, a data frame d_j , $j \in \{1, \dots, J\}$, can be expressed as the convolution of an object, f , and a point spread function (PSF), s_j . Localizing such a subfield to be centered at a point (x_k, y_k) , $k \in \{1, \dots, K\}$, and using a square (\square) as a superscript to denote the subfielding, we get

$$d_{jk}^{\square}(x, y) = [f_k^{\square} * s_{jk}](x, y) + n_{jk}^{\square}(x, y), \quad (1)$$

where n_{jk}^{\square} is an additive noise term with Gaussian statistics. The spatial coordinates, (x, y) , will henceforth be dropped except when explicitly needed for clarity, as will their frequency domain counterparts, (u, v) .

For multi-frame data with additive Gaussian noise statistics, there exists a Maximum-Likelihood estimate, indicated with a caret ($\hat{\cdot}$), of the object¹⁶. Using capital letters for Fourier transforms and prepending a low-pass noise filter, H_k , we can write

$$\begin{aligned} \hat{F}_k^{\square} &= H_k \frac{\sum_j D_{jk}^{\square} S_{jk}^*}{\sum_{j'} |S_{j'k}|^2} \\ &= \sum_j D_{jk}^{\square} \frac{H_k S_{jk}^*}{\sum_{j'} |S_{j'k}|^2}, \end{aligned} \quad (2)$$

where an asterisk ($*$) used as a superscript denotes complex conjugation. For the last expression, we could move

the filter and the j' sum inside the j sum because they are not dependent on j . The resulting fraction,

$$Q_{jk} = \frac{H_k S_{jk}^*}{\sum_{j'} |S_{j'k}|^2}, \quad (3)$$

is in effect an *inverse OTF* of D_{jk}^{\square} and the multi-frame deconvolution of subfield k can be written as

$$\hat{F}_k^{\square} = \sum_j D_{jk}^{\square} Q_{jk}. \quad (4)$$

The corresponding *inverse PSF* is then

$$q_{jk} = \mathfrak{F}^{-1}\{Q_{jk}\}, \quad (5)$$

where \mathfrak{F} denotes a Fourier transform operation and \mathfrak{F}^{-1} its inverse. Deconvolution of multiple frames D_{jk}^{\square} can then be realized as co-adding the results from independent convolutions with the inverse PSF kernels, i.e.,

$$\hat{f}_k^{\square} = \sum_j \hat{f}_{jk}^{\square} = \sum_j d_{jk}^{\square} * q_{jk}. \quad (6)$$

Convolution is a linear operation, so if we expand the inverse PSFs in some basis functions $\{g_{jm}\}$, we can write

$$\begin{aligned} \hat{f}_{jk}^{\square} &= d_{jk}^{\square} * q_{jk} \\ &= d_{jk}^{\square} * \left(\sum_m \alpha_{jmk} g_{jm} \right) \\ &= \sum_m (\alpha_{jmk} d_{jk}^{\square}) * g_{jm}, \end{aligned} \quad (7)$$

where α_{jmk} are expansion coefficients. The proper choice of basis functions is described in Sect. 2 B.

In practice, for anisoplanatic data, isoplanatic image formation is only an approximation at any useful subfield size. The inverse PSFs vary continuously between the sample points and the deconvolution should take that into account. Following Ref. 14, we now substitute $a_{jm}(x, y)$, functions of x and y like the d_j frames, for the α_{jmk} coefficients. See Sect. 2 C for details on the interpolation and normalization of these coefficient surfaces. We can then write, for the full FOV,

$$\hat{f}_j(x, y) = \sum_m (a_{jm}(x, y) \cdot d_j(x, y)) * g_{jm} \quad (8)$$

and

$$\hat{f} = \sum_j \sum_m (a_{jm} \cdot d_j) * g_{jm}. \quad (9)$$

B. Karhunen–Loève decomposition of inverse PSFs

In Ref. 15, K–L transforms were used to find the most efficient set of orthogonal basis functions for expansion of a set of PSFs. We will do the same for the inverse PSFs for a single frame, j . Our derivation is similar to the one in Ref. 17.

K–L basis functions are orthonormal and uncorrelated. Clearly that is not the case for the inverse PSFs themselves, the correlation matrix, \mathbf{C} , of which has elements of the form

$$C_{kk'} = \sum_{x,y} q_{jk} q_{jk'}. \quad (10)$$

Defining \mathbf{Q} as the matrix, the k th column of which is the pixel values of q_{jk} , Eq. (10) can be written in matrix form as

$$\mathbf{C} = \mathbf{Q}^T \mathbf{Q}, \quad (11)$$

where T used as a superscript denotes matrix transpose. Defining $\mathbf{1}$ as the identity matrix and using standard linear algebra, Eq. (11) can be diagonalized to the form

$$\mathbf{1} = (\mathbf{\Lambda}^{-1/2} \mathbf{E}^T \mathbf{Q}^T) (\mathbf{Q} \mathbf{E} \mathbf{\Lambda}^{-1/2}) = \mathbf{G}^T \mathbf{G}, \quad (12)$$

where the columns of \mathbf{E} are the eigenvectors of \mathbf{C} , $\mathbf{\Lambda}^{-1/2}$ is the diagonal matrix of the reciprocals of the square roots of the corresponding eigenvalues, and \mathbf{G} is defined as the second parenthetical expression. In analogy with the definition of \mathbf{Q} , column m of \mathbf{G} contains the pixel values of an orthonormal basis function,

$$g_{jm} = \lambda_{mm}^{-1/2} \sum_k E_k q_{jk}, \quad (13)$$

where E_k is column k of \mathbf{E} . We call the $\{g_{jm}\}_{m=1}^K$ set of functions the *K–L kernels* for frame j .

In Ref. 18, many useful properties of K–L transforms are derived and demonstrated. Using all K K–L kernels, expansions can reproduce the K inverse PSFs perfectly. The K–L kernels is the most efficient set of basis functions in the sense that a truncated expansion, using the subset of $M < K$ kernels corresponding to the largest eigenvalues, minimizes the RMS residuals of the truncation. This efficiency property is particularly useful since we need to represent both the complicated wings of short-exposure PSFs and the centroid shifts from the geometrical distortions. The choice of M depends on the desired accuracy. K–L kernels corresponding to very small eigenvalues can be expected to mostly encode measurement noise and can be omitted with no significant loss of accuracy. In particular, g_{jm} for $m : \lambda_{mm} = 0$ are undefined and should never be used.

C. Continuous coefficient surfaces

The coefficient surfaces, $a_{jm}(x, y)$, should be fitted to or interpolated between the coefficients given at the grid points, α_{jkm} at (x_k, y_k) . It is not strictly necessary that the sample point PSFs are reproduced exactly but they do need to be reproduced to within their expected errors and make smooth transitions between the sample points. In Ref. 13, for AO and long exposures, where the PSF shapes are anisotropic and depend mainly on the direction vector to the AO lock point, a fit in polar coordinates is used but it is noted that the choice of method

depends on the context. In Refs. 14 and 15, low-order x and y polynomials are fitted, expecting mainly changes of FWHM of long-exposure PSFs.

If the unit integral of the PSFs is not preserved between the sample points, there are spurious intensity variations in the restored image. Photometric accuracy requires that the coefficient surfaces are normalized with respect to a unit image frame, $d_{jm} \equiv 1$, so that

$$1 \equiv \sum_m^M [a_{jm} * g_{jm}](x, y); \quad \forall j, x, y. \quad (14)$$

This is easily ensured by, separately for each j , dividing each coefficient surface with the quantity corresponding to the right hand side of Eq. (14), calculated from the non-normalized surfaces.

3. Demonstration

In this section we demonstrate the space-variant deconvolution method as implemented in the interpreting data processing language ANA²⁰. On 2 May 2003, the SST targeted the symmetrical sunspot in NOAA Active Region 0346²¹ through a narrowband (FWHM 1 nm) G-band interference filter (430.5 nm). The AO²² system was used and the instrumental setup was such that the plate scale is 0''.041/pixel and the diffraction limited resolution $\lambda/D = 0''.09$. The data set used here consists of five pairs of phase diverse images collected within 8 s. PSFs were estimated on an approximately equidistant grid with $K = 9 \times 13 = 117$ sample points separated about 70 pixels by use of Joint Phase Diverse Speckle (JPDS) implemented as MFBD with linear equality constraints¹. The size of the overlapping subfields is 128×128 pixels. The procedure is described in detail in Ref. 2. Figure 1 shows the restoration of one such data set, using the method presented in this paper with $M = 20$ K–L kernels.

The fading of details toward the edges of the FOV are artifacts from windowing used for the convolutions in Eq. (9), implemented with FFTs. In order to avoid high-frequency wraparound artifacts, the FFT operations were not performed on the d_j directly, but on $(d_j - \langle d_j \rangle)w + \langle d_j \rangle$, where angular brackets denote spatial averaging and w is a window function that is unity except at the edges, where a cosine taper brings it smoothly to zero. To compensate slightly, the figure does not show f but $(f - \langle f \rangle)/w + \langle f \rangle$. It is the division by w , close to zero at the edges, that is responsible for the intensity artifacts at the very edges, particularly the corners, of the figure.

We use data from one of the five focused frames to illustrate PSFs, inverse PSFs, and K–L kernels. The estimated PSFs, as well as the corresponding inverse PSFs, are shown in Fig. 2. The K–L kernels, g_{jm} , are shown in Fig. 3. The first K–L kernel represents the core of an almost symmetric and centered inverse PSF. The following few K–L kernels encode off-center and elongated

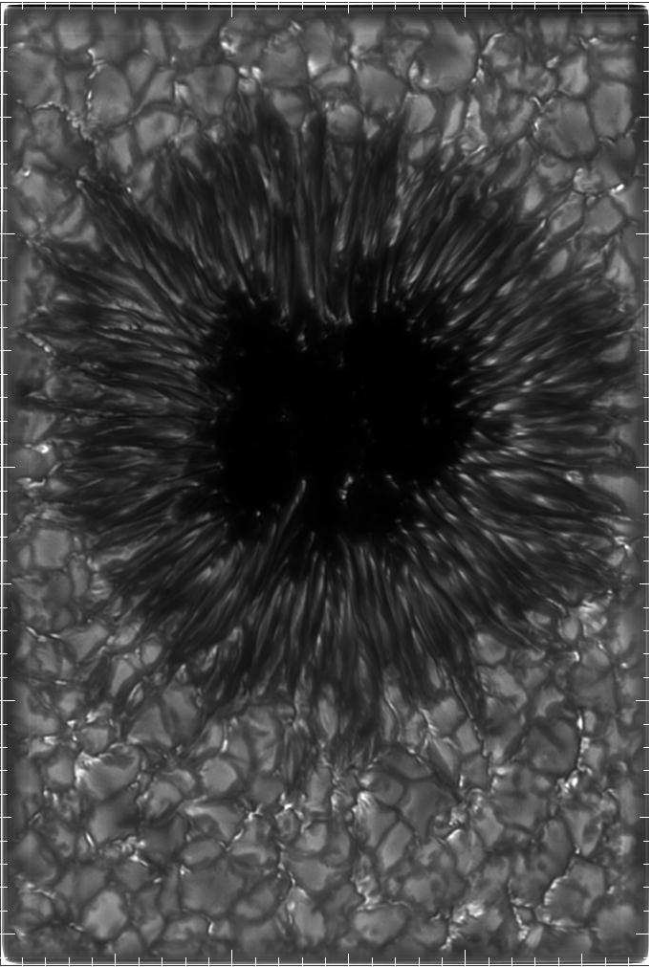


Fig. 1. Sunspot image restored using the method described in this paper. PSFs were estimated with phase diversity from five pairs of simultaneous exposures in and out of focus. The image was restored using only the focused data frames along with their PSFs. The tick marks are $1''$ apart.

cores. The remaining K–L kernels deal with the wings and, increasingly, with noise. In the figure, the K–L kernels are individually scaled to use the available dynamical range. In reality, they rapidly decrease in contrast as well as importance. In Fig. 4 we show one inverse PSF and compare it with expansions using different M . This particular inverse PSF is so off-centered that five terms are needed to recreate the core. $M = 10$ K–L kernels are probably sufficient to capture the important features. This agrees well with the eigenvalues plotted in Fig. 5, that have dropped more than two orders of magnitude for $m = 10$. However, we have not evaluated the expansions of the entire set of inverse PSFs in this respect. We used expansion with $M = 20$ for the demonstration data.

Figure 6 shows one sample expansion coefficient as a function of position in the FOV. The piecewise constant interpolation illustrates the original coefficient array with discrete values at the grid points, used for entire sub-

fields when doing mosaicking. For the continuous surface, when modeling the random variations over the FOV of anisoplanatic short-exposure PSFs, we use interpolation rather than a fit (cf. Sect. 2C). We get smooth variations without ringing artifacts by use of a damped bicubic interpolation method (the formula of Ref. 19 with $\alpha = -0.5$).

In Fig. 7 we show a part of the image in Fig. 1, deconvolved in several different ways. The FOV is selected so that it is centered on a line between two rows of PSF locations, as defined by the centers of the subfields used in the wavefront sensing step. The top tiles, Fig. 7(1)–(5), show the raw data. Figure 7(a) is restored using the space-variant inverse filtering deconvolution method presented in this paper, while (b) is a mosaic of subfields individually deconvolved with inverse filtering. As the two methods use the same five raw data frames, the same PSFs, and similar inverse filtering methods, the two restorations are very similar as expected. The only visible differences appear along the horizontal center line, where some features are slightly more blurred in (b) because of the blending of discontinuities at the interfaces between adjacent subfields. This effect can be easier understood by inspection of (c) and (d), which are single-frame versions of (a) and (b), respectively, based on the raw data shown in tile (2). In order to emphasize the mismatches along the subfield divider line that are avoided with the new method, the mosaic in (d) was done using mosaic window functions without taper or overlap. Comparison of (c) and (d) shows that the major effect of the space-variant deconvolution is not in the deblurring as much as in the avoidance of discontinuities. This is emphasized in the difference image in (e), where horizontal displacements show up as black-white signatures and vertical displacements as breaks in continuous features. Closer scrutiny also reveals subtle differences in residual blurring, consistent with the continuous versus discrete transition between the neighboring PSFs. Comparison of (a) and (c) also demonstrates the trade-off involved in multi-frame versus single-frame deconvolution: while (a) has better SNR than (c), its resolution is not quite as good. The latter effect is partly caused by residual geometrical mismatches between the five raw data frames, which would be expected to be reduced further when an optimum method for coefficient surface interpolation/fitting is determined for this kind of data.

4. Discussion

We have developed and implemented a method for space-variant, multi-frame deconvolution of high-resolution solar images. The demonstration data set is of very good quality, yet the improvement compared to mosaicking is clearly visible in Fig. 7. The method is useful for MFBD and Multi-Object MFBD (MOMFBD)⁴ processing. It is more time consuming than mosaicking but the extra time is insignificant in comparison to processing of large MOMFBD data sets.

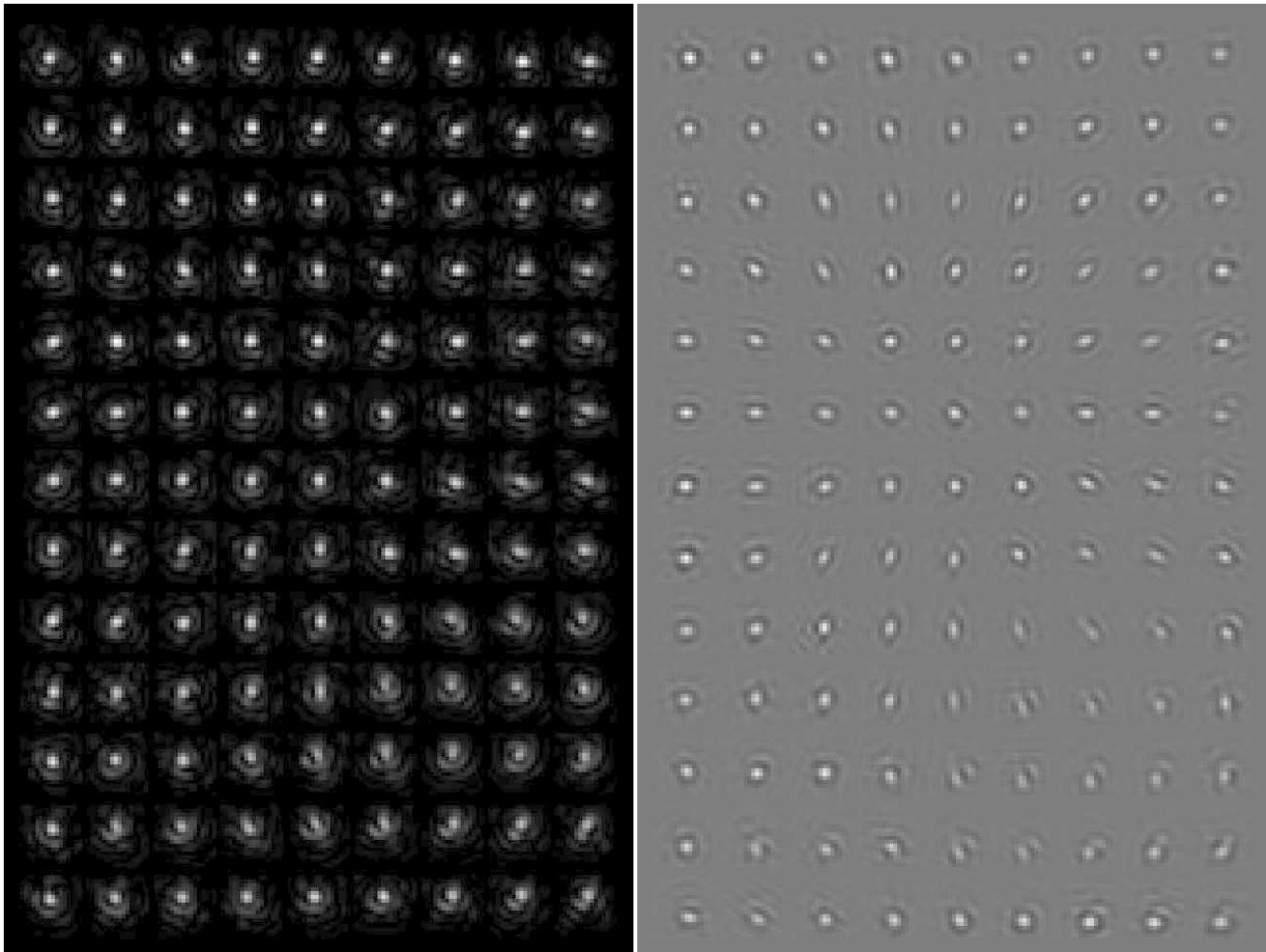


Fig. 2. Blurring and deblurring kernels from one of the focused frames, magnified and mosaicked to show their position in the FOV of Fig. 1. **Left:** The estimated PSFs, s_{jk} , displayed with gamma set to emphasize the wings. **Right:** The corresponding inverse PSFs, q_{jk} .

The wavefront sensing part of MFBD methods can now be decoupled from the deconvolution part. Failed PSF estimates can be left out of the surface fits without leaving gaps in the restored image. For large data sets, time may be saved by measuring PSFs first on a sparse grid, and then filling in measurements based on some criterion for accepted differences between neighboring PSFs.

In Ref. 13, it was noted that the proper way of interpolating the coefficient surfaces must be context driven and a parametric fit in polar coordinates was used. Here, we have used damped bicubic interpolation. Fig. 6 suggests that a low-order parametric surface would fit the coefficient array quite well and that residuals would encode estimation errors rather than important variations over the FOV. However, surfaces corresponding to other coefficients have less regular appearances. It should be clear, that the variation of the PSFs is not known between the grid points, and that the PSFs are only estimates. So, while smooth transitions between the grid points is cer-

tainly an improvement to the piecewise constant approximation implied in mosaicking, it may be even better to ignore some of the variation, corresponding to errors or noise. PSFs estimated from MFBD data without PD are generally less well determined than those estimated from PD data, which implies that the optimum choice of interpolation method might differ between different data sets, even with closely related processing algorithms. One could investigate the proper choice by estimating PSFs on a much denser grid and compare the resulting coefficient arrays with the interpolated surfaces. We expect such experimenting with denser grids and different interpolation methods will be faster and easier when this algorithm has been incorporated as an option in the MOMFBD C++ code²³.

The choice of M is also context dependent. For applications where the main interest is in the morphology, smaller M may be appropriate than for photometrically critical data.

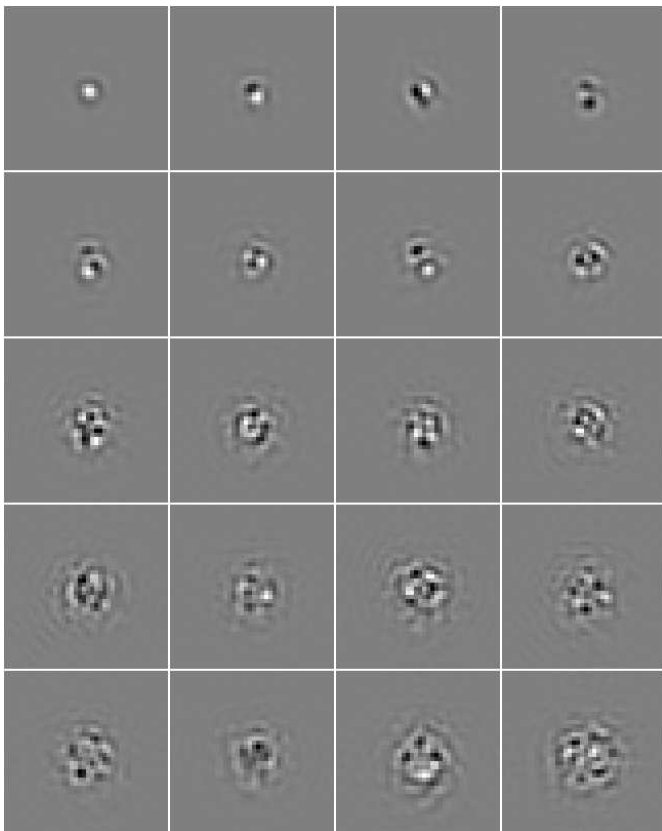


Fig. 3. The first 20 K-L kernels, g_{jm} , corresponding to the inverse PSFs of Fig. 2. Top row, left-right: $m = 1, 2, 3, 4$; second row: $m = 5, 6, 7, 8$; etc. The kernels are individually scaled to use the available dynamical range.

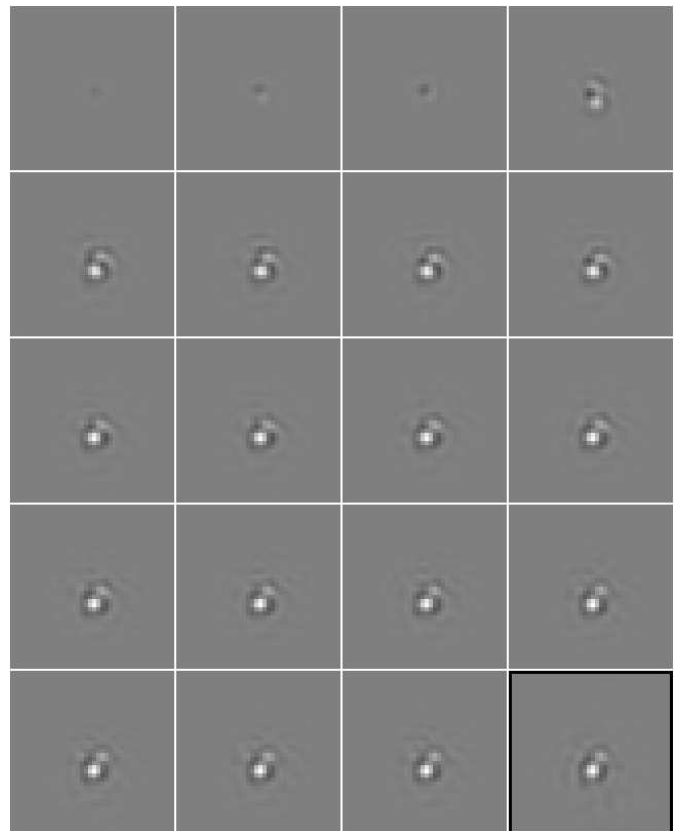


Fig. 4. One inverse PSF, q_{jk} , from Fig. 2, bottom right tile, framed. The other tiles show expansions, left-right: $M = 1, 2, 3, 4$; etc. Compare Fig. 3.

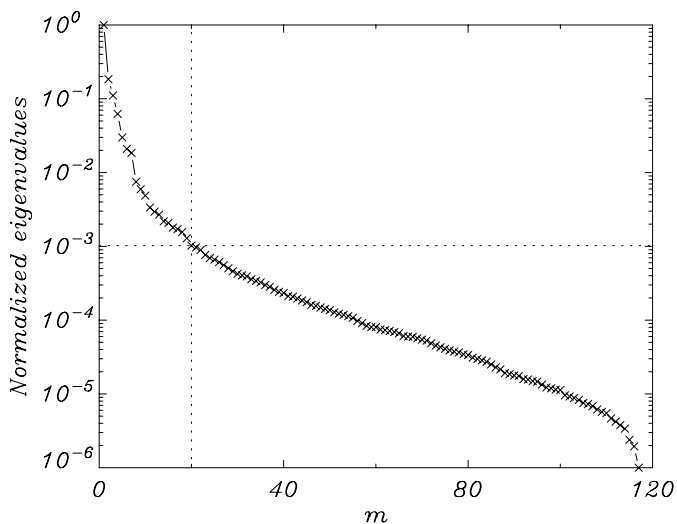


Fig. 5. The (normalized) eigenvalues corresponding to the K-L kernels in Fig. 3. The dotted lines indicate the $M = 20$ cutoff used for the demonstration.

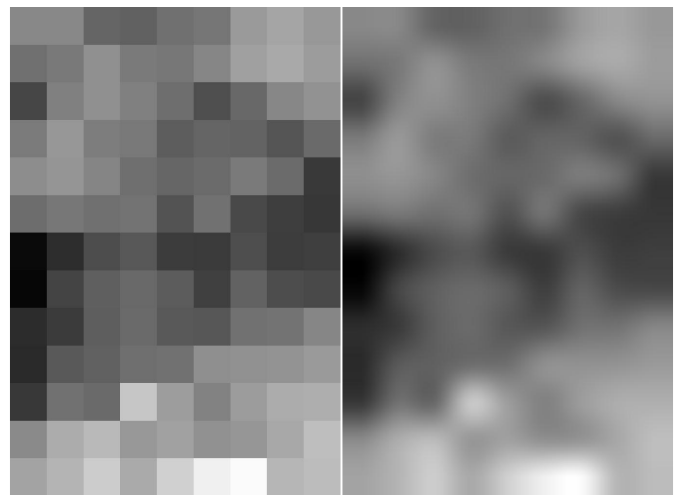


Fig. 6. Sample expansion coefficient surface, $a_{jm}(x, y)$, coded as shades of gray and covering the entire FOV of Fig. 1. These maps correspond to the inverse PSFs of Fig. 2 and the fourth K-L kernel of Fig. 3. **Left:** Piecewise constant; **Right:** Damped bicubic interpolation.

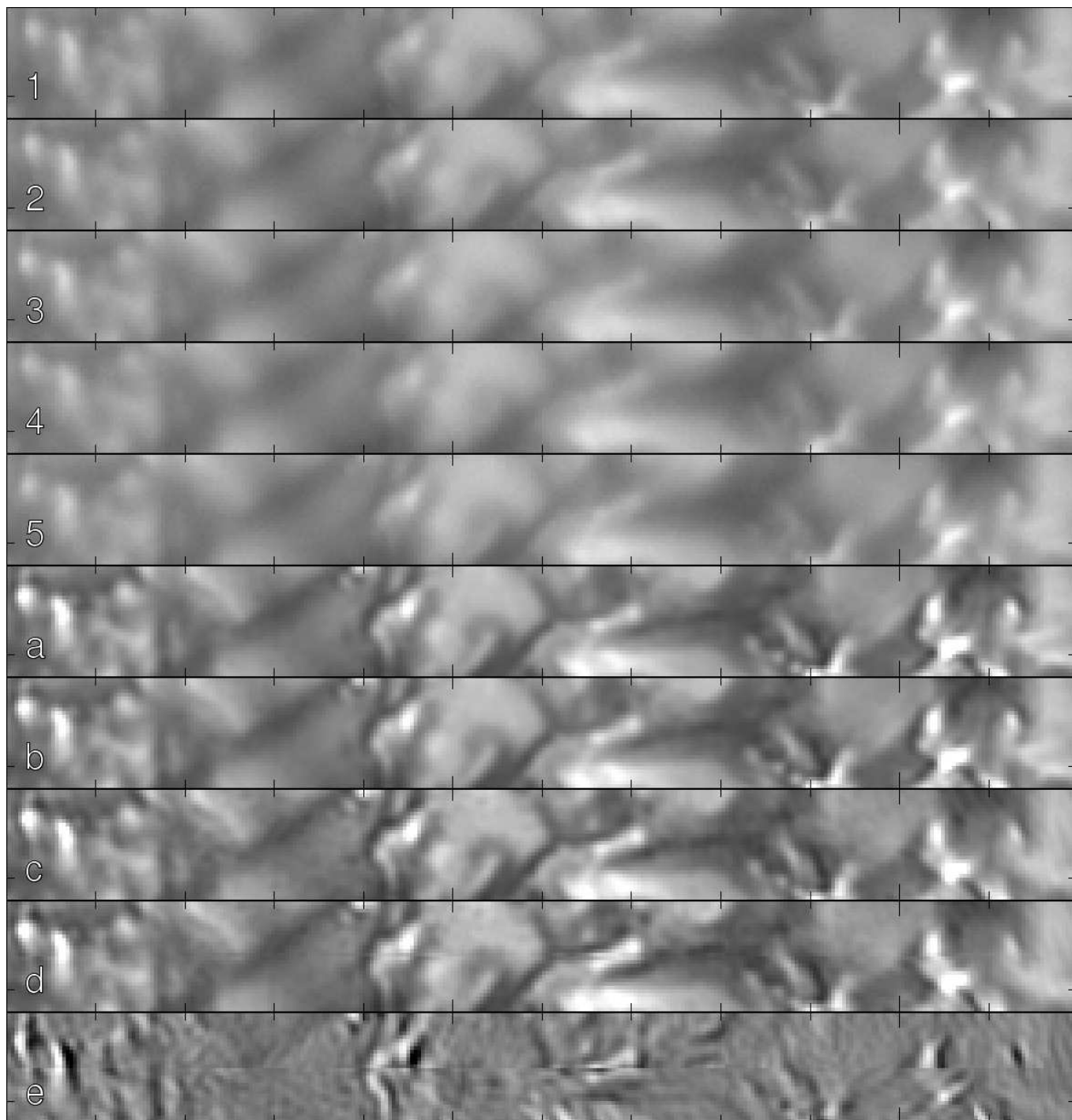


Fig. 7. Restoration along the interface between adjacent rows of mosaic subfields. The FOV is part of Fig. 1. **(1)–(5)** Raw data. **(a)** Restoration using multi-frame, space-variant inverse filtering; **(b)** Mosaic of inverse-filtered subfields; **(c)** Single-frame restoration using space-variant inverse filtering; **(d)** Mosaic of single-frame, space-variant inverse filtering using window functions without taper or overlap; **(e)** Difference between (c) and (d), emphasizing the discontinuities between adjacent rows of subfields in the mosaic. Note mismatch both in position and in contrast over the subfield boundary. (There are similar mismatches between columns, although not as noticeable here.) The tick marks are $1''$ apart.

For the purposes of the method described here, the H_k filter of Eq. (3) can be any low-pass filter. One obvious choice is a Wiener filter. In our implementation, we have used Scharmer’s optimum low pass filter²⁴. The important point is that filter variations over the FOV (because of varying SNR) are part of the inverse PSFs and therefore encoded also in the smoothly varying representation based on the interpolated coefficient maps, $a_{jm}(x, y)$.

For the examples in this paper, the full-frame FFTs were performed on the full, rectangular FOV. This minimizes the bookkeeping but may not be optimal in terms of computing time, particularly if the array dimensions have large prime factors. It would however be easy to implement this in terms of mosaicking of square subfields with power-of-2 sizes. In contrast to mosaicking with varying PSFs, this should not result in any mismatches between subfields, because the mosaicking would in this case be of subfields convolved with identical K–L kernels.

The introduction mentions that existing space-variant PD algorithms^{5,6} are extremely time consuming. It would be an interesting challenge to use the approach presented in this paper to make a faster implementation, covering all varieties of MFBD.

Acknowledgments

I am grateful to Richard Shine of LMSAL for help with 2D interpolation in ANA and to Michiel van Noort for reading drafts of this paper and suggesting improvements. This research was supported by NSF under grant IIS ITR 03-24816. The Swedish 1-m Solar Telescope is operated on the island of La Palma by the Institute for Solar Physics of the Royal Swedish Academy of Sciences in the Spanish Observatorio del Roque de los Muchachos of the Instituto de Astrofísica de Canarias.

References

1. M. G. Löfdahl, “Multi-frame blind deconvolution with linear equality constraints,” in *Image Reconstruction from Incomplete Data II*, P. J. Bones, M. A. Fiddy, and R. P. Millane, eds., vol. 4792 of *Proc. SPIE*, pp. 146–155 (2002).
2. M. G. Löfdahl and G. B. Scharmer, “Phase diverse speckle inversion applied to data from the Swedish 1-meter solar telescope,” in *Innovative Telescopes and Instrumentation for Solar Astrophysics*, S. Keil and S. Avakyan, eds., vol. 4853 of *Proc. SPIE*, pp. 567–575 (2003).
3. R. A. Gonsalves, “Phase retrieval and diversity in adaptive optics,” *Optical Engineering* **21**(5), 829–832 (1982).
4. M. van Noort, L. Rouppe van der Voort, and M. G. Löfdahl, “Solar image restoration by use of multi-frame blind deconvolution with multiple objects and phase diversity,” *Solar Physics* **228**(1–2), 191–215 (2005).
5. R. G. Paxman, B. J. Thelen, and J. H. Seldin, “Correction of anisoplanatic blur by using phase diversity,” in *Adaptive Optics in Astronomy*, M. A. Ealey and F. Merkle, eds., vol. 2201 of *Proc. SPIE*, pp. 1066–1067 (1994).
6. R. A. Gonsalves, “Nonisoplanatic imaging by phase diversity,” *Optics Letters* **19**, 493–495 (1994).
7. O. von der Lühse, “Speckle imaging of solar small structure: I. Methods,” *Astronomy & Astrophysics* **268**, 374–390 (1993).
8. G. B. Scharmer, K. Bjelksjö, T. K. Korhonen, B. Lindberg, and B. Pettersson, “The 1-meter Swedish solar telescope,” in *Innovative Telescopes and Instrumentation for Solar Astrophysics*, S. Keil and S. Avakyan, eds., vol. 4853 of *Proc. SPIE*, pp. 341–350 (2003).
9. M. G. Löfdahl and G. B. Scharmer, “Wavefront Sensing and Image Restoration from Focused and Defocused Solar Images,” *Astronomy & Astrophysics Supplement Series* **107**, 243–264 (1994).
10. G. B. Scharmer, D. S. Brown, L. Pettersson, and J. Rehn, “Concepts for the Swedish 50-cm Vacuum Solar Telescope,” *Applied Optics* **24**(16), 2558–2564 (1985).
11. R. G. Paxman, J. H. Seldin, M. G. Löfdahl, G. B. Scharmer, and C. U. Keller, “Evaluation of Phase-Diversity Techniques for Solar-Image Restoration,” *Astrophysical Journal* **466**, 1087–1099 (1996).
12. J. G. Nagy and D. P. O’Leary, “Fast iterative image restoration with a spatially varying PSF,” in *Advanced Signal Processing: Algorithms, Architectures, and Implementations VII*, F. T. Luk, ed., vol. 3162 of *Proc. SPIE*, pp. 388–399 (1997).
13. T. R. Lauer, “Deconvolution with a spatially-variant PSF,” in *Astronomical Data Analysis II*, J.-L. Starck and F. D. Murtagh, eds., vol. 4847 of *Proc. SPIE*, pp. 167–173 (2002).
14. C. Alard, “Image subtraction using a space-varying kernel,” *Astronomy & Astrophysics Supplement Series* **144**, 363–370 (2000).
15. R. Lupton, J. E. Gunn, Ž. Ivezić, and G. R. Knapp, “The SDSS imaging pipelines,” in *Astronomical Data Analysis Software and Systems X*, F. R. Harnenden Jr., F. A. Primini, and H. E. Payne, eds., vol. 238 of *ASP Conf. Ser.*, pp. 269–278 (2001).
16. R. G. Paxman, T. J. Schulz, and J. R. Fienup, “Joint estimation of object and aberrations by using phase diversity,” *Journal of the Optical Society of America A* **9**(7), 1072–1085 (1992).
17. N. Roddier, “Atmospheric wavefront simulation using Zernike polynomials,” *Optical Engineering* **29**(10), 1174–1180 (1990).
18. M. S. Vogeley and A. S. Szalay, “Eigenmode analysis of galaxy redshift surveys. I. Theory and methods,” *Astrophysical Journal* **465**, 34–53 (1996).
19. S. K. Park and R. A. Schowengerdt, “Image Reconstruction by Parametric Cubic Convolution,” *Computer Vision, Graphics, and Image Processing* **23**, 258–272 (1983).
20. R. A. Shine, L. Z. Porter, Z. Frank, J. B. Gur-

- man, D. Pothier, and S. Ferguson, *A User's Guide to ANA*, Lockheed Palo Alto Research Laboratory (1988). See also ana.lmsal.com.
21. Institute for Astronomy of the University of Hawaii, "AR map 2 May, 2003," www.solar.ifa.hawaii.edu/ARMaps/archive.html.
 22. G. B. Scharmer, P. Dettori, M. G. Löfdahl, and M. Shand, "Adaptive optics system for the new Swedish solar telescope," in *Innovative Telescopes and Instrumentation for Solar Astrophysics*, S. Keil and S. Avakyan, eds., vol. 4853 of *Proc. SPIE*, pp. 370–380 (2003).
 23. M. van Noort and M. Löfdahl, "Multi-Object Multi-Frame Blind Deconvolution," Public domain C++ code available at www.momfbd.org (2005).
 24. M. G. Löfdahl, T. E. Berger, R. A. Shine, and A. M. Title, "Preparation of a Dual Wavelength Sequence of High-Resolution Solar Photospheric Images using Phase Diversity," *Astrophysical Journal* **495**, 965–972 (1998).